

Improving Precision in Kinematic Weak Lensing with MIRoRS: Model-Independent Restoration of Reflection Symmetries

CHRISTOPHER HOPP ¹ AND DAVID WITTMAN ¹

¹*Department of Physics & Astronomy, University of California, Davis, CA 95616*

ABSTRACT

We present a novel, model-independent technique for fitting the cross-component of weak lensing shear, γ_{\times} , along a line of sight by combining kinematic and photometric measurements of a single lensed galaxy. Rather than relying on parametric models, we fit for the shear parameter that best transforms the velocity field to restore its underlying symmetries, while also incorporating photometric data for the change in position angle due to shear. We first validate our technique with idealized mock data, exploring the method's response to variations in shear, position angle, inclination, and noise. On this idealized mock data, our combined kinematic and photometric model demonstrates superior performance compared to traditional parametric or kinematic-only approaches. Subsequently, we apply our method to a dataset of 358 halos from the Illustris TNG simulations, achieving a notable reduction in the uncertainty of γ_{\times} to 0.039, marking a substantial improvement over previous analysis of the dataset with a parametric model. Finally, we introduce an outlier rejection method based on Moran's I-test for spatial autocorrelation. Identifying and filtering out halos with spatially correlated residuals reduces the overall uncertainty to 0.028. Our results underscore the efficacy of combining kinematic and photometric data for weak lensing studies, providing a more precise and targeted measurement of shear along an individual line of sight.

1. INTRODUCTION

Weak gravitational lensing provides a robust method for probing the mass distribution of the universe (see [Bartelmann & Schneider \(2001\)](#) for a comprehensive review and [Bartelmann & Maturi \(2017\)](#) for a more contemporary treatise). As the light from an extended background source travels through the potential well of a foreground lens, it is distorted such that the image observed carries information about the underlying mass distribution of the lens. This distortion manifests in two primary effects: convergence and shear. Convergence, typically denoted κ , produces an isotropic scaling of the image, maintaining the shape while scaling the size. Shear, denoted γ , distorts the shape of the image, elongating along one axis and compressing in an orthogonal direction. Determining the intrinsic size of a source is typically difficult, thus the primary information available is in the ellipticity and orientation of the image.

In the weak lensing regime, these effects are small, typically with ellipticity distortions less than 1% ([McKay](#)

[et al. 2001](#)). Meanwhile, the intrinsically wide distribution of unlensed galaxy orientation and ellipticity, or shape noise, overwhelms the signal of a single source. In traditional weak lensing, shape noise is overcome by using a statistical ensemble of sources to search for this systematic distortion. While the uncertainty in the shape of any single source is large, it is presumed that there is no preferential orientation of an unlensed source ensemble. Averaging over a large number of sources, of order $\sim 10^4$ in cluster-galaxy lensing ([Umetsu 2020](#); [Umetsu et al. 2014](#)) and up to $\sim 10^7$ in cosmic shear studies ([Troxel et al. 2018](#)), is required to achieve a desirable signal-to-noise ratio.

With no a priori knowledge of the shape and orientation of an unlensed galaxy, traditional weak lensing will always be plagued by shape noise. However, some source galaxies possess sufficient symmetries in their velocity field such that the light observed is not completely devoid of information on the unlensed condition of the galaxy. From the equivalence principle, it is known that lensing effects are independent of photon wavelength. Thus, the velocity field of a galaxy will also show the effects of shearing. Under idealized conditions, an unlensed disk galaxy has perpendicular kinematic axes and

displays symmetry in its velocity field along its major axis and antisymmetry along its minor axis. These symmetries are broken under shear and it was first recognized by Blain (2002) that this deviation produces an observable that can be used to infer the shear parameter from a single galaxy.

This work was extended by Morales (2006) and significant progress has since been made in the subfield of Kinematic Lensing (henceforth KL). The most common approach involves fitting a parametric model of a sheared velocity field to observations. This approach was most recently explored by Donet & Wittman (2023, hereafter DW23), where an uncertainty in $\gamma_{\times} \approx 0.08$ was found across a sample of 358 halos from Illustris TNG simulations (Nelson et al. 2019). This uncertainty represents an improvement over traditional weak lensing methods, but it remains larger than the typical available signal, underscoring the need for further refinement.

These parametric modeling techniques are reliant upon the form of the velocity profile chosen. True rotation curves do not often match such an idealized model. While KL offers potential improvement over traditional weak lensing techniques on a per-source basis, an ensemble of galaxies is still required to overcome the variability in galaxy kinematic morphology, or kinematic shape noise (Gurri et al. 2020). However, de Burgh-Day et al. (2015, dBD15) proposed a model-independent approach, using only the symmetry properties of a galaxy. Later, it was shown by DiGiorgio et al. (2021, DiG21) that explicitly including the offset in the position angle between the kinematic and photometric axes, in conjunction with a kinematic model, reduces statistical uncertainty in the inferred shear parameter by a factor of 2–6. We seek to refine and extend these works.

Our approach takes inspiration from dBD15, but has some fundamental differences. Starting from an observed velocity field, we transform the field back to the source plane through translation, rotation, and lensing shear. When transformed with true parameter values, the symmetry (antisymmetry) under reflections across the major (minor) axis will be restored. Performing these reflections and then transforming back to the detector frame gives two new velocity fields, one for each symmetry transformation. These fields are then combined into a single nonparametric model and compared to the original data to compute a residual and a likelihood to be optimized. We also incorporate some of the methods of DiG21. In our likelihood function, we include a term from the difference between the observed photometric and modeled kinematic axes.

We first characterize our approach using idealized mock data to explore its response and limitations. Af-

ter the initial testing, we applied our model to a more realistic dataset, comprised of 358 halos from the Illustris TNG simulations. This is the same dataset used by DW23, allowing for a direct comparison between our method and their parametric approach. Finally, we demonstrate an objective method for discarding outliers whose velocity fields do not follow the idealized assumptions. We utilized a Moran’s I-test for spatial autocorrelation to search for patterns in the residuals indicating unmodeled physical effects.

The paper is structured as follows: in §2 we will discuss weak lensing and its effects on observables, §3 will outline our approach, and §4 will cover results and discussion.

2. WEAK LENSING

The theory of gravitational lensing in general, and weak lensing in particular, is well-established in the literature (Bartelmann & Schneider 2001; Bartelmann & Maturi 2017; Umetsu 2020). Light from a background source, following a geodesic, will be deflected as it travels through the potential well of a massive body. This deflection will produce a distorted image, encoding information from the intervening mass distribution. For the purpose of this paper, we will limit our discussion to the weak lensing regime of small deflections. We will also assume that the characteristic size of the lensing mass distribution is small compared to the distances along the geodesic and adopt a thin-lens approximation of the lens.

Under these assumptions, the transformation between the source and the observed image can be expressed as

$$\mathcal{A} = \begin{pmatrix} 1 - \kappa - \gamma_+ & -\gamma_{\times} \\ -\gamma_{\times} & 1 - \kappa + \gamma_+ \end{pmatrix}, \quad (1)$$

where γ_+ and γ_{\times} represent the two components of the shear vector γ and κ gives the convergence. In our convention, the shear vector is oriented perpendicular to the line connecting the source and lens, as projected onto the plane of the sky. This transformation actually represents the inverse of the shearing operation, taking an image in the detector plane back to the source plane. Lensing of a source to the observed image is done through the inverse operation \mathcal{A}^{-1} ,

$$\mathcal{A}^{-1} = \mu \begin{pmatrix} 1 - \kappa + \gamma_+ & \gamma_{\times} \\ \gamma_{\times} & 1 - \kappa - \gamma_+ \end{pmatrix}, \quad (2)$$

where the prefactor $\mu = ((1-\kappa)^2 - |\gamma|^2)^{-1}$ gives the magnification, and the magnitude of total shear is given by $|\gamma|^2 = \gamma_+^2 + \gamma_{\times}^2$. Examining this tensor gives insight into the effect of each component. Convergence produces an

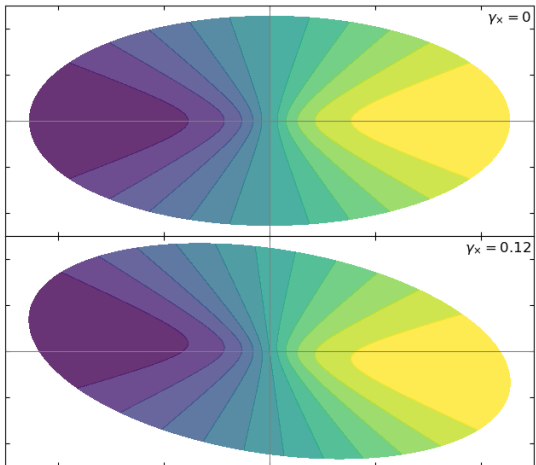


Figure 1. Velocity field of a non-sheared galaxy (top) and galaxy with $|\gamma_x| = 0.12$ shear applied (bottom) from a lens along the $y = x$ line from the source. The sheared galaxy displays a notable loss of symmetry in its kinematic field as well as an apparent rotation in its morphology.

isotropic focusing of the image while both components of shear produce anisotropic effects. The first component, γ_+ , stretches and compresses the image along the coordinate axes. This produces an elliptical image of an otherwise circular source, but is indistinguishable from the inherent ellipticity of the unlensed object. The second component, γ_x , shears the object along the $y = x$ axis. These components can be expressed in terms of the total magnitude of shear and angle α between the shear vector and coordinate axes,

$$\gamma_x = |\gamma| \sin(2\alpha) \quad (3)$$

$$\gamma_+ = |\gamma| \cos(2\alpha). \quad (4)$$

We can simplify this transformation by recognizing that κ , producing only isotropic effects, will not impact the symmetry properties of the galaxy. Neglecting κ gives

$$\mathcal{A} = \begin{pmatrix} 1 - \gamma_+ & -\gamma_x \\ -\gamma_x & 1 + \gamma_+ \end{pmatrix}, \quad (5)$$

$$\mathcal{A}^{-1} = \mu \begin{pmatrix} 1 + \gamma_+ & \gamma_x \\ \gamma_x & 1 - \gamma_+ \end{pmatrix}. \quad (6)$$

2.1. Distortion of Observables

At the heart of the KL method lies the fact that under a weak lensing shear transformation, a disk galaxy will lose its inherent symmetries. As can be seen in Figure 1, the non-sheared field exhibits a symmetry in its velocity field about the major axis and an antisymmetry across the minor axis. After applying the cross-component of

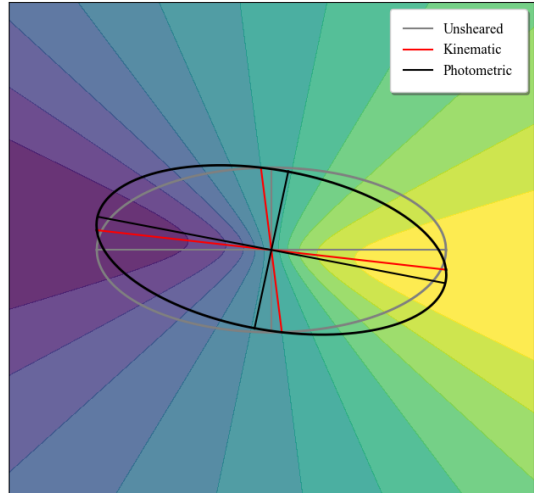


Figure 2. Pre and post-lensing kinematic and photometric axes corresponding to an elliptical isophote overlaid on the sheared velocity field. Prior to lensing, both the kinematic and photometric axes are aligned (gray). After lensing, the isophote will remain elliptical with orthogonal photometric axes (black). For small values of γ_+ , the transformation of the isophote can be well-modeled as an ellipse rotated by an angle θ as shown in Equation 17. The kinematic axes (red), on the other hand, do not remain orthogonal. The discrepancy between the kinematic and photometric major and minor axes is given by Equation 20 and Equation 21 respectively.

shear ($\gamma_x = 0.12$ in this case), these symmetries are both lost. We use this loss of symmetry to fit for the unknown shear parameter directly by finding the transformation of the sheared field that restores the symmetry.

We can also take advantage of the fact that the kinematic and photometric axes are transformed differently, as seen in Figure 2. Our approach largely mirrors the work of DiG21, correcting for some inconsistencies that do not affect their ultimate findings. An isophote of the unlensed galaxy can be modeled as an ellipse in the source (x,y) coordinates,

$$1 = q^2 x^2 + y^2, \quad (7)$$

where q is the ratio between minor and major axes, $q = b/a$, in the source plane. We are interested in the image produced in the detector coordinates, (x', y') . Transforming from the source plane to the observed image in the detector plane through Equation 5, $\mathbf{x} = \mathcal{A}\mathbf{x}'$, gives

$$x = x'(1 - \gamma_+) - y'\gamma_x \quad (8)$$

$$y = y'(1 + \gamma_+) - x'\gamma_x. \quad (9)$$

The isophote in the detector plane is then

$$1 = q^2(x'(1 - \gamma_+) - y'\gamma_x)^2 + (y'(1 + \gamma_+) - x'\gamma_x)^2. \quad (10)$$

Note, q is the axis ratio in the source plane and is not directly observable. We will address the observed axis ratio later, with Equation 16. In the weak lensing regime, we expect the shear parameters to be small, allowing us to expand and drop any quadratic terms. Combining like terms yields

$$1 \approx q^2(1-2\gamma_+)x'^2 + (1+2\gamma_+)y'^2 - 2\gamma_\times x'y'(1+q^2). \quad (11)$$

Next, we will approximate the transformation of the isophote as a rotation rather than a shear. Under a counterclockwise rotation Equation 7 becomes

$$1 = q'^2(x' \cos \Delta\theta + y' \sin \Delta\theta)^2 + (y' \cos \Delta\theta - x' \sin \Delta\theta)^2. \quad (12)$$

Here, the observed axis ratio, q' , is the same in both the source and detector frames. We denote the photometric rotation angle as $\Delta\theta$ to emphasize that this rotation is the change in photometric position angle due to lensing. In the weak lensing regime we expect this rotation angle to be small and thus use small angle approximations to first order,

$$1 \approx q'^2 x'^2 + y'^2 - 2x'y'\Delta\theta(1-q'^2). \quad (13)$$

Comparing coefficients from Equation 11 and Equation 13 provides relationships between the rotation angle, θ , and the shear parameter γ_\times as well as relationships between the axis ratio in each frame. Looking first at the y'^2 term,

$$1 = (1 + 2\gamma_+), \quad (14)$$

we see that $\gamma_+ \approx 0$ for the transformation to be modeled as a rotation. For our purposes, this is achieved by orienting the the galaxy axes such that the shear vector aligns with γ_\times . In a real observation, γ_+ will typically be small, but non-zero. We address this in §4.2.1.

We can also now revisit Equation 5 and Equation 6. Under the current approximations of weak lensing, and by defining our coordinate system such that $\alpha = 45^\circ$ and thus $|\gamma| = \gamma_\times$, the transformation matrices are then

$$\mathcal{A} = \begin{pmatrix} 1 & -\gamma_\times \\ -\gamma_\times & 1 \end{pmatrix}, \quad \mathcal{A}^{-1} = \mu \begin{pmatrix} 1 & \gamma_\times \\ \gamma_\times & 1 \end{pmatrix}. \quad (15)$$

With $\gamma_+ = 0$, the x'^2 term,

$$q'^2 = (1 - 2\gamma_+)q^2, \quad (16)$$

indicates the observed axis ratio, $q' = q$, the source axis ratio. Finally, the $x'y'$ term gives us

$$\Delta\theta = \frac{1 + q'^2}{1 - q'^2} \gamma_\times. \quad (17)$$

This is the change in position angle of the photometric axes due to lensing. However, the pre-lensed condition of both the axis ratio and position angle is unknown.

Turning our attention to the transformation of the kinematic axes, it is evident in Figure 2 that the velocity field cannot be modeled as a simple rotation. If we consider a point on the major axis of the unlensed galaxy, $(x, 0)$, that point will be transformed to $(x', y') = (\mu(1 + \gamma_+)x, \mu\gamma_\times x)$. The kinematic axis angle, post-lensing, is then displaced by an angle

$$\Delta\phi_{\text{maj}} = \tan^{-1} \left(\frac{\gamma_\times}{1 + \gamma_+} \right) \approx \gamma_\times, \quad (18)$$

while the minor axis is displaced

$$\Delta\phi_{\text{min}} = \frac{\pi}{2} - \tan^{-1} \left(\frac{1 - \gamma_+}{\gamma_\times} \right) \approx -\gamma_\times. \quad (19)$$

Knowing the displacement of each set of axes from the unlensed condition, in which we assume the axes are aligned, allows us to infer the shear from the difference between the photometric and kinematic axes. Defining our coordinate system such that the unlensed galaxy has its axes aligned with the coordinate axes, the change in position angles reduces to the observed position angles in the detector frame. Looking first at the major axis, the difference $\Delta_{\text{maj}} = \theta' - \phi'$ is given by

$$\Delta_{\text{maj}} = \left(\frac{1 + q^2}{1 - q^2} \gamma_\times \right) - \gamma_\times = \frac{2\gamma_\times q^2}{1 - q^2}. \quad (20)$$

Meanwhile, the difference between observed minor axes is

$$\Delta_{\text{min}} = \frac{2\gamma_\times}{1 - q^2}. \quad (21)$$

We can then solve for γ_\times in terms of the difference in angle,

$$\gamma_{\times, \text{maj}} = \frac{(1 - q^2)}{2q^2} \Delta_{\text{maj}} \quad (22)$$

$$\gamma_{\times, \text{min}} = \frac{(1 - q^2)}{2} \Delta_{\text{min}}. \quad (23)$$

3. METHODS

3.1. Overview

We modify and combine the approaches of dBD15 and DiG21, using both kinematic and photometric data to fit for the cross-component of shear, γ_\times .

We first characterize our methods with tests on idealized mock data. Galaxy parameters for shear, position angle, inclination, and noise are varied to explore the performance and limitations of the approach. We then analyzed a set of 358 galaxies selected from Illustris TNG100-1 simulations (Nelson et al. 2019). These halos are all at $z = 0$ and have an expected shear value $\gamma_\times = 0$. This data was used by DW23, allowing for a

direct comparison between our methods and parametric modeling.

Finally, the residual maps for each halo are analyzed for spatial autocorrelation using a Global Moran's I test. Correlated patterns in the residuals indicate unmodeled physical effects and, as such, provide a method for screening the results.

3.2. Direct Shear Mapping

The Direct Shear Mapping (DSM) technique was first developed by dBD15. By exploiting the effect of weak lensing on the intrinsic symmetry of the velocity field of a galaxy, they were able to fit for the shear parameter, γ_{\times} , in a completely model-independent fashion. While conceptually similar, our implementation is materially different, with an emphasis on accurately capturing the model uncertainties.

The velocity field of a rotationally-supported disk galaxy is expected to have intrinsic symmetry across its major axis and antisymmetry across its minor, with the major and minor axes being orthogonal. After lensing, the axes are no longer orthogonal, but have a separation given by the difference between Equation 18 and Equation 19,

$$\theta_{\perp} \approx \frac{\pi}{2} \pm 2\gamma_{\times}. \quad (24)$$

Fitting for γ_{\times} with only this separation of the axes is possible, but does not fully utilize the information available. Instead, DSM uses velocity data across the entire face of the galaxy to quantify the loss of symmetry.

The loss of symmetry is unique to the effects of γ_{\times} . Thus, we can fit for γ_{\times} using Equation 5 by finding the transformation that restores this symmetry. This fit will also depend on nuisance parameters for the central velocity, (x, y) coordinate of the centroid, and position angle, ϕ , in the source plane. All relevant parameters are given in Table 1.

The general approach is to use a simulated annealing optimization to fit for these parameters. A set of parameters is assumed and used to transform the field. More in-depth discussion on these transformations is described below. The transformed field is compared to the original field to compute a per-pixel χ^2 value and likelihood.

The transformations, shown in Figure 3, start with the velocity field data and associated per-pixel uncertainty field in the observed detector frame.

1. The field is first translated from its observed position, (x_c, y_c) , to the detector origin. Future operations (rotation, shear) are implemented about

Table 1. Fitting parameters

Parameter	Symbol	Unit
Shear	γ_{\times}	-
Central Velocity	V_c	km/s
Position Angle	ϕ	deg
Centroid	(x_c, y_c)	pixel

this origin. Note that (x_c, y_c) are then fitting parameters, and not simply an observation.

2. Next, we apply a shear transformation to restore the unlensed fields in the source coordinates, $[x, y]$. With the correct parameters for (x_c, y_c) and γ_{\times} , the intrinsic symmetry of the field will be restored at this point.
3. In order to properly implement the two symmetry transformations, the galaxy axes must be aligned with the coordinate axes. Thus, the unsheared fields are rotated by a parameter for the position angle in the source plane, ϕ .
4. Two independent symmetry transformations are applied to the velocity field: a reflection across the major axis and an inversion across the minor axis. Each transformation is performed separately, resulting in distinct model fields for the major and minor axes. To account for the antisymmetry across the minor axis, the inversion consists of a reflection followed by a sign change. To derive the expression for the minor-axis model field, the central velocity parameter, V_c , is subtracted from both the reflected and model fields, and the sign is inverted, giving $V_{\text{model}} - V_c = -(V_{\text{reflect}} - V_c)$, which simplifies to $V_{\text{model}} = 2V_c - V_{\text{reflect}}$.
5. These transformed fields should be identical to the original field if the correct parameters are used in the transformations (assuming, of course, intrinsic symmetry). The fields are averaged into a single model. This model is then transformed back into the detector plane by applying the inverse of each operation, rotation, shear, translation.
6. Once back in the detector plane, the transformed model is compared to the data to compute a residual and likelihood.

The actual implementation of this algorithm involves a sequence of coordinate transformations, applied to both

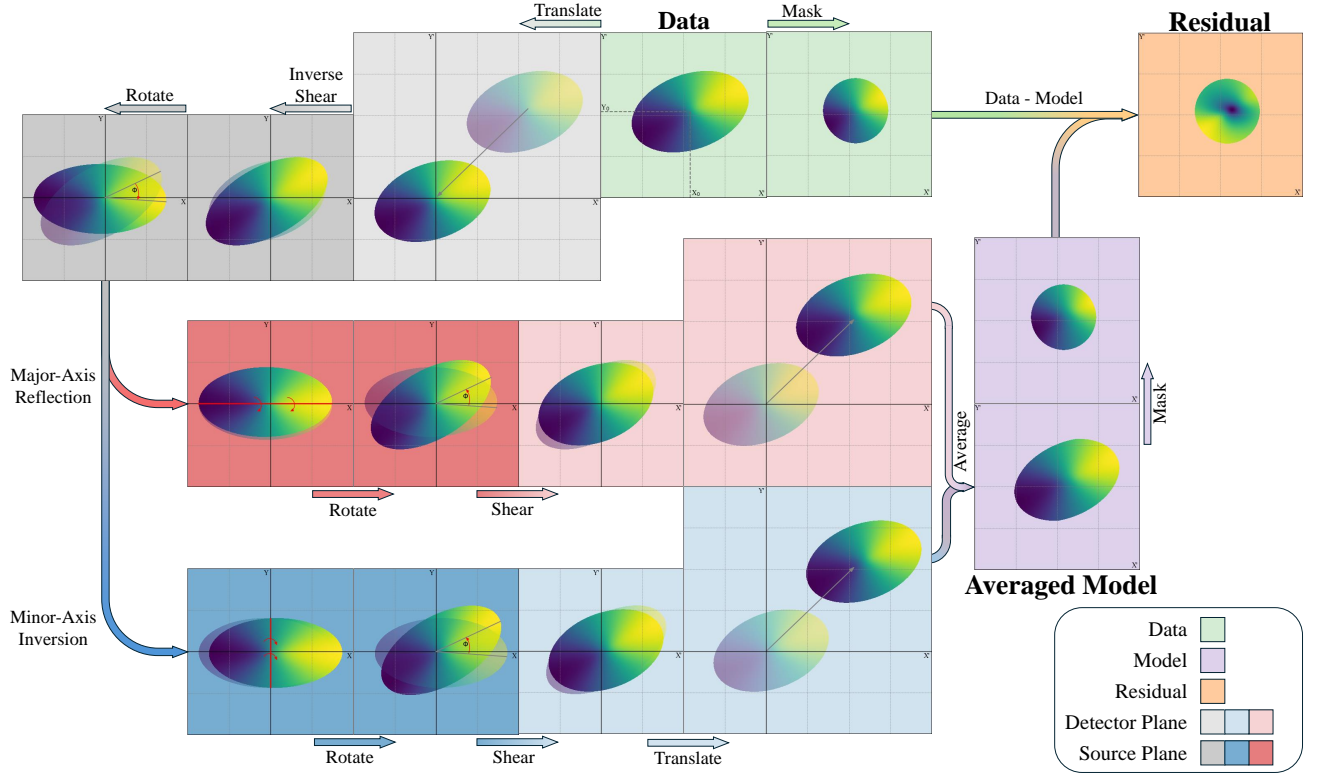


Figure 3. Illustration of the nonparametric fitting algorithm. Starting in the detector frame (light background), data (green) is first masked around a central pixel. To create a model, the raw data is translated to the detector origin and inverse shear is applied, bringing the image into the source plane (dark background). A clockwise rotation orients the galaxy axes with the coordinate axes. Two symmetry transformations are done independently; a reflection about the major axis (red) and an inversion about the minor (blue) using Equation 33. Rotation and shear are then reapplied to bring the images back to the source plane where they are translated back to the original position. The two separate images are combined into a single model (purple) and masked with the same mask as applied to the data. The difference between the model and the data produces the residual (orange). Here, the data has an applied shear, $\gamma_x = 0.15$ and position angle $\phi = 30^\circ$ while the model transformations use $\gamma_x = 0.12$ and $\phi = 29^\circ$ so a non-zero residual is produced.

the velocity and uncertainty fields. The likelihood produced here is combined with a term from the displacement of the photometric axes, covered in the next section.

3.3. Photometric Axes

To constrain the shear parameter from photometric data, we need to calculate the difference between the detector-plane kinematic and photometric axes. The photometric position angle in the detector plane is directly observable. Fitting for the kinematic position angle, on the other hand, is more troublesome. These complications are dealt with in [Krajinovic et al. \(2006\)](#), however, uncertainties in kinematic position angle from this method range from 3° for rotational velocities exceeding 100 km/s to 17° for rotational velocities lower than 100 km/s ([Krajinović et al. 2011](#)).

Instead, we choose to utilize the source-plane kinematic position angle fitting parameter, ϕ , to predict the

observed photometric position angle, θ' . The detector position angle can be expressed by $\phi' = \tan^{-1}\left(\frac{y'}{x'}\right)$, where the coordinates are expressed in the lensed frame. We can then transform these coordinates into the source plane, substituting $x = \cos \phi$ and $y = \sin \phi$, to give the detector-frame kinematic position angle as a function of fitted quantities,

$$\phi'_{\text{maj}} = \tan^{-1}\left(\frac{\sin \phi + \gamma_x \cos \phi}{\cos \phi + \gamma_x \sin \phi}\right). \quad (25)$$

Combining with Equation 20 and solving for the photometric major axis position angle, we have

$$\theta'_{\text{maj}} = \phi'_{\text{maj}} + \frac{2q^2\gamma_x}{(1-q^2)}. \quad (26)$$

This value can be compared to the observed photometric position angle to produce a χ^2 value and associated term in our likelihood function.

3.4. Optimizer

We utilize the `scipy.optimize.dual_annealing` optimizer to fit for our function parameters. The dual annealing algorithm is a global optimization method that combines the stochastic approach of simulated annealing with a local minimizer. Simulated annealing searches for the global minimum of a function by exploring the solution space through random changes. The optimizer uses a “temperature” to dictate the aggressiveness of its global search. Early on, at high temperature, there is considerable leniency to explore the parameter space. Over time, the temperature decreases, simulating the process of annealing in metallurgy, and the optimizer is more restricted in its search. This global search is coupled with a local search algorithm to explore the space at higher resolution. This approach allows the algorithm to escape local minima and approach the global minimum, making it particularly effective for complex, multimodal function optimization problems. In our case, we used the truncated Newton optimizer to search the local landscape. We found that overall the fit was not sensitive to initial annealing temperature or number of iterations, but did require a dedicated global search algorithm. Using a local minimizer alone would settle into a local minimum without finding the global minimum.

We also implemented MCMC analysis with `emcee` (Foreman-Mackey et al. 2013) and found similar results, but at increased computation time. Because we are interested in ensemble variances rather than the variances within the fit of a particular halo, we opted for the computational efficiency of `dual_annealing`. MCMC did help to provide valuable information about the nature of the likelihood surfaces we were exploring and would be a useful tool in analyzing individual halos and their associated uncertainties.

3.5. Fitting Algorithm

3.5.1. Kinematic Fitting

The function to be optimized is the negative log-likelihood. This likelihood is calculated from both the kinematic and photometric data with their associated uncertainties. For the kinematic calculation, we start with the observed velocity field and uncertainty map. The data is pre-processed to ensure all galaxies in the analysis have the same rotation direction and any missing pixels have their uncertainty set to infinity.

The likelihood depends on the residual between a transformed model and the data so, first, a data region must be defined. The transformations to create the model, particularly the shear transformation, distort the field in such a manner that pixels with no data from outside the field can be brought into the model.

This necessitates using a mask region small enough that reasonable transformation parameters cannot introduce these NaN pixels. This region is selected by taking the pixels within a prescribed radius of the center of the field. Note, while the centroid location is a fitting parameter, the data region must be established prior to the fitting so that all residual calculations done by the optimizer take the difference from the same set of data.

The original velocity and error fields are then transformed to create a model via the transformations shown in Figure 3. Rotations are done through the standard rotation and inverse rotation matrices,

$$\mathcal{R} = \begin{pmatrix} \cos \phi & -\sin \phi \\ \sin \phi & \cos \phi \end{pmatrix}, \quad \mathcal{R}^{-1} = \begin{pmatrix} \cos \phi & \sin \phi \\ -\sin \phi & \cos \phi \end{pmatrix}, \quad (27)$$

while the shearing operations happen via Equation 15, stated here for completeness,

$$\mathcal{A} = \begin{pmatrix} 1 & -\gamma_{\times} \\ -\gamma_{\times} & 1 \end{pmatrix}, \quad \mathcal{A}^{-1} = \mu \begin{pmatrix} 1 & \gamma_{\times} \\ \gamma_{\times} & 1 \end{pmatrix}. \quad (28)$$

The two symmetry operations are similarly implemented with the matrices

$$\mathcal{T}_x = \begin{pmatrix} 1 & 0 \\ 0 & -1 \end{pmatrix}, \quad \mathcal{T}_y = \begin{pmatrix} -1 & 0 \\ 0 & 1 \end{pmatrix}. \quad (29)$$

These matrices are combined into two overall transformation operations and applied to both the data and the error maps. Applying the transformations in a single step requires only a single interpolation, rather than an interpolation for each operation. These operations do not generally commute, so care must be taken to perform the operations in the correct sequence. First, the maps are translated to the detector origin and inverse shear is applied to bring the observed field back to the source plane. Next, a clockwise rotation to align the major axis with the x-axis. The fields are then reflected across the coordinate axes, creating two sets of velocity and error maps. Each of these maps is then rotated counterclockwise and the shear re-applied. This brings the images back to the detector plane where they are translated back to the original centroid and averaged into a single model to compute a residual. Combined, these transformations are

$$\mathcal{M}_{\text{major}} = \mathcal{A}\mathcal{R}\mathcal{T}_x\mathcal{R}^{-1}\mathcal{A}^{-1}, \quad (30)$$

$$\mathcal{M}_{\text{minor}} = \mathcal{A}\mathcal{R}\mathcal{T}_y\mathcal{R}^{-1}\mathcal{A}^{-1}. \quad (31)$$

While we have discussed these transformations as being done to the fields, in reality they are acting on the coordinates. The new coordinate grid to be interpolated

onto, including translations, is then

$$\begin{pmatrix} x_{\text{new}} \\ y_{\text{new}} \end{pmatrix} = \mathcal{M} \begin{pmatrix} x_{\text{data}} - x_c \\ y_{\text{data}} - y_c \end{pmatrix} + \begin{pmatrix} x_c \\ y_c \end{pmatrix}, \quad (32)$$

where \mathcal{M} is the transformation for either the major or minor axis reflection.

Once this transformed grid is established, cubic spline interpolation is used to produce the new velocity and error maps. The velocity field from the minor axis reflection is then scaled by the central velocity to account for the antisymmetry,

$$V_y = 2V_c - V_{\text{reflect}}. \quad (33)$$

The two velocity fields are then averaged to produce a model,

$$V_{\text{model}} = \frac{V_x + V_y}{2}, \quad (34)$$

while the uncertainty in the model is computed from the two uncertainty maps,

$$\sigma_{\text{model}} = \sqrt{\sigma_x^2 + \sigma_y^2}. \quad (35)$$

The overall per-pixel uncertainty is the quadrature sum of uncertainties in both model and data,

$$\sigma_i = \sqrt{\sigma_{\text{model}}^2 + \sigma_{\text{data}}^2}. \quad (36)$$

The fields are then masked at the same position as the data and a per-pixel χ^2 is computed,

$$\chi_i^2 = \frac{(V_{i,\text{model}} - V_{i,\text{data}})^2}{\sigma_i^2}. \quad (37)$$

With a per-pixel χ^2 , our likelihood function to be maximized is

$$\mathcal{L} = \prod_i \frac{1}{\sqrt{2\pi\sigma_i^2}} e^{-\chi_i^2/2}. \quad (38)$$

Taking the log-likelihood gives

$$\ln \mathcal{L} = -\frac{1}{2} \sum_i (\chi_i^2 + \ln \sigma_i^2 + \ln 2\pi). \quad (39)$$

In the optimization process, each iteration will involve comparisons between models that have been created from transformations of potentially different regions of the original data with different uncertainties. To account for this variability in the model uncertainty, the normalization term, $\ln \sigma_i^2$, must be retained in the likelihood function. The third term in the expression, $\ln 2\pi$, is a constant and can be safely dropped, leaving

$$\ln \mathcal{L} = -\frac{1}{2} \sum_i (\chi_i^2 + \ln \sigma_i^2). \quad (40)$$

This differs from dBD15 in that no 180° rotation operation is done and the χ^2 is computed from an averaged model instead of simply summing over total pixels. On the first issue of the rotation, we can express such a rotation by

$$\mathcal{T}_{\text{rot}} = \begin{pmatrix} -1 & 0 \\ 0 & -1 \end{pmatrix}. \quad (41)$$

This is simply the negative of the identity matrix, the full transformation matrix is then

$$\mathcal{M}_{\text{rot}} = -\mathcal{A}\mathcal{R}\mathcal{I}\mathcal{R}^{-1}\mathcal{A}^{-1} = -\mathcal{I}. \quad (42)$$

This holds for any shear parameter or position angle, thus rotations are independent of shear. Rotation operations could help constrain the other parameters in the problem—the center position and central velocity—but this would need to be done separately from the fitting of the shear parameter and implemented as a prior. Including the rotation operation in our model would increase the noise without adding any information.

On the second issue of creating an averaged model versus separately computing a χ^2 for the individual fields produced by each reflection, we find that summing over the pixels of the fields separately underestimates the error due to the individual fields not being truly independent. Consider the case of the reflection across the major axis alone. The residual is the difference between data and model, but the model itself is built from the data. If we look at a simplified, 2-pixel image, with one upper and one lower pixel, identified with subscripts U and L respectively, the χ^2 value (using unit uncertainty in the data) would be

$$\chi^2 = (M_U - D_U)^2 + (M_L - D_L)^2, \quad (43)$$

where M and D refer to model and data. However, the model is just the reflection of the data such that $M_{U/L} = D_{L/U}$. With this, the double-counting is evident

$$\chi^2 = (M_U - D_U)^2 + (D_U - M_U)^2 \quad (44)$$

$$= 2(M_U - D_U)^2 = 2(M_L - D_L)^2. \quad (45)$$

Alternatively, rather than reflecting the data, the operation can be thought of as a folding of the data across its axis demonstrating that the number of true comparisons is only half the pixels. The same concept holds true for the reflection across the minor axis. By summing over the entirety of pixels in each transformed field separately, the number of independent data points is artificially inflated. Instead, we choose to average over two transformations which creates a unique comparison for each pixel in the image.

3.5.2. Photometric Fitting

To the likelihood function in Equation 40, we add a contribution from the photometric position angle. To characterize the photometric axes of a galaxy, we begin by computing the centroid of the intensity distribution. While the derivation of the angular offset in the kinematic and photometric axes does presume a collocated centroid for the two observations, we choose to calculate the photometric centroid independently rather than use the fitting parameters for the kinematic centroid, (x_c, y_c) . This saves computation time, calculating a single value for the photometric position angle rather than a calculation at each iteration. It also prevents the photometric observation from having an influence on the kinematic fitting parameters for (x_c, y_c) . The centroid coordinates (\bar{x}, \bar{y}) are calculated using the first-order raw moments, given by

$$\bar{x} = \frac{M_{10}}{M_{00}}, \quad \bar{y} = \frac{M_{01}}{M_{00}}, \quad (46)$$

where $M_{ij} = \sum_{x,y} x^i y^j I(x, y)$ denotes the raw moment and $I(x, y)$ is the intensity at pixel coordinates (x, y) .

Next, we compute the covariance matrix,

$$\text{Cov}[I(x, y)] = \begin{pmatrix} \frac{M_{20}}{M_{00}} - \bar{x}^2 & \frac{M_{11}}{M_{00}} - \bar{x}\bar{y} \\ \frac{M_{11}}{M_{00}} - \bar{x}\bar{y} & \frac{M_{02}}{M_{00}} - \bar{y}^2 \end{pmatrix}. \quad (47)$$

Diagonalization yields eigenvalues and eigenvectors corresponding to the length and orientation of the major and minor axes. The axis ratio is inferred from the square root of the eigenvalues' ratio.

With the axis ratio, we can calculate a model value for the photometric position angle from Equation 26. The axis ratio measurement introduces uncertainty in the model value which must be accounted for. The uncertainty in the model term is calculated through standard propagation of errors

$$\sigma_{\theta', \text{model}} = \sqrt{\left(\frac{4q\gamma_x}{(1-q^2)^2} \sigma_q \right)^2}. \quad (48)$$

Combining this term with the uncertainty in the observed position angle gives the total error in the photometric angle,

$$\sigma_{\theta'}^2 = \sigma_{\theta', \text{model}}^2 + \sigma_{\theta', \text{obs}}^2. \quad (49)$$

The uncertainties in observed position angle and axis ratio are determined directly from the distribution of position angles and axis ratios in our data sample, as shown in Subsection 4.1. A χ^2 value is then calculated

$$\chi_{\theta'}^2 = \frac{(\theta'_{\text{model}} - \theta'_{\text{obs}})^2}{\sigma_{\theta'}^2}, \quad (50)$$

and added to complete the likelihood function

$$\ln \mathcal{L} = -\frac{1}{2} \left(\sum_i (\chi_i^2 + \ln \sigma_i^2) + \chi_{\theta'}^2 + \ln \sigma_{\theta'}^2 \right). \quad (51)$$

Again, the normalization term, $\ln \sigma_{\theta'}^2$, must be retained to account for changes in model uncertainty.

3.6. Data Selection

3.6.1. Idealized Mock Data

To characterize the performance of our nonparametric approach, we first create a set of idealized mock data for both the velocity and intensity fields. The intensity field is described by an exponentially decaying profile,

$$I(r) = I_0 \exp\left(\frac{-2.99r}{r_{80}}\right) \sec(i), \quad (52)$$

where r is the radial coordinate in the source plane, r_{80} is the radius enclosing 80% of the light, i is the inclination angle, and I_0 gives the central intensity. The factor of 2.99 is required to enforce the r_{80} condition.

For the velocity field we model an infinitely thin disk with an arctangent profile with the major axis aligned along the x -axis,

$$V(r) = \frac{2}{\pi} V_{\text{max}} \arctan\left(\frac{r}{r_0}\right) \sin(i) \frac{x}{|x|} + V_c, \quad (53)$$

where r_0 is the scale radius independent of the intensity, V_{max} is the asymptotic velocity, and V_c the central velocity of the galaxy.

Gaussian noise is added to both fields. For the intensity field, the amplitude of the noise is flat across the observation. For the velocity field, the noise is assumed to go as $I^{-1/2}$,

$$\sigma_V = \delta_V \sqrt{\frac{I_0}{I}}, \quad (54)$$

where δ_V sets the noise level at the central pixel.

Both fields are then interpolated from the source plane coordinates onto a grid which has been transformed by a shear parameter, γ_x , major axis position angle, ϕ , and inclination i .

3.6.2. Illustris TNG

After characterization with idealized data, we then analyze a set of 358 subhalos from a $z = 0$ snapshot of the Illustris TNG100-1 (Nelson et al. 2019) magnetohydrodynamical simulations. These halos were originally analyzed with parametric methods by DW23 and we refer the reader to their methods for an in-depth discussion on data selection. The general selection criteria required all samples to have a total mass within 10% of

$1.4 \times 10^{12} M_{\odot}$, with $\geq 40\%$ ($\leq 30\%$) of the stellar mass to be within the disk (bulge).

The subhalos were all oriented according to the principal axis of the moment of inertia tensor calculated from the stellar particles. The longest principal axis was aligned along the coordinate x-axis as the major axis while the second largest principal axis was aligned as the minor axis. The galaxies were also arranged to have a clockwise rotation.

3.7. Outlier Rejection

For a well-fit model, residuals are expected to be primarily due to uncorrelated noise. Spatially correlated patterns in residuals can be the result of a poorly fit parameter or from unmodeled physical effects such as spiral arms, bars, or warps. We use a Global Moran’s I-test for spatial autocorrelation (Moran 1948) to quantify the extent to which these patterns are present in the residuals, identifying halos with a poor fit. Examining residuals for spatial autocorrelation is not a new technique (Goodchild 1986), but has been largely limited to fields outside of astronomy. In using the Moran’s I-test, we seek to quantify the effectiveness of our modeling, but also to explore the utility of spatial autocorrelation in characterizing residuals.

To implement the Moran’s I-test, we first compute the residuals by subtracting the model values from the observed values. These residuals are then normalized by their combined errors, resulting in a standardized residuals image. The Moran’s I statistic is then calculated to measure spatial autocorrelation, using the package `PySAL.esda` (Rey & Anselin 2007). Specifically, we use the Queen contiguity method (named for the directions a Queen may move in chess) to create a spatial weight matrix, where each element w_{ij} is 1 if locations i and j are neighbors (sharing a border or vertex) and 0 otherwise. The Moran’s I statistic is given by

$$I = \frac{N \sum_i \sum_j w_{ij} (v_i - \bar{v})(v_j - \bar{v})}{W \sum_i (v_i - \bar{v})^2} \quad (55)$$

where N is the number of pairwise comparisons (number of pixels squared), W is the sum of all weights, v_i (v_j) is the residual velocity value at location i (j), and \bar{v} is the mean velocity residual. This formula quantifies the degree to which similar or dissimilar values cluster together in space. A Moran’s I value greater than zero indicates positive spatial autocorrelation (clustering), while a value less than zero indicates negative spatial autocorrelation (dispersion). A value near zero suggests a random spatial pattern. By computing the p-value associated with Moran’s I, we assess the statistical significance of the observed spatial autocorrelation against

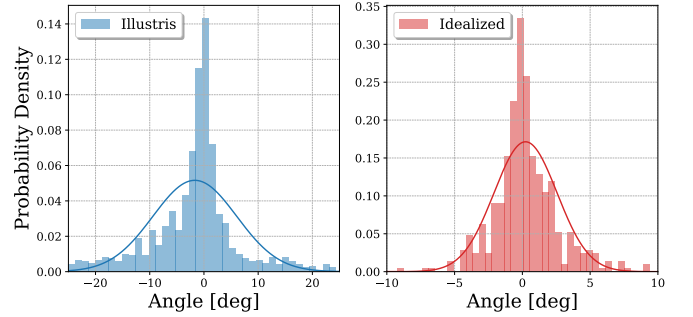


Figure 4. Distribution of errors in fitting of photometric axes. The width of the best-fit Gaussian is 7.7° for the Illustris sample and 2.3° for the idealized data. Both results are more sharply peaked than indicated by the Gaussian fit.

a null hypothesis of complete spatial randomness. This statistical framework enables us to identify and quantify spatially correlated residuals, taking a low p-value as an indication of spatial correlation in the residuals and a potentially problematic fit.

4. RESULTS AND DISCUSSION

4.1. Axis Errors

Our likelihood function contains a term involving the uncertainty in the photometric position angle and the axis ratio, so we begin by quantifying those errors. We apply our axis fitting code to the full data sample and calculate uncertainties from the resulting distributions. These empirical uncertainties are then used in the likelihood function.

First, we consider the position angles. The subhalos from Illustris are aligned with the primary principal axis of their inertia tensor along the x-axis. If we take this as a proxy for a “true” position angle of 0° , the distribution of fitted position angles represents the error in the measurement. Likewise, the position angle in the idealized mock data is known, so we are able to cre-

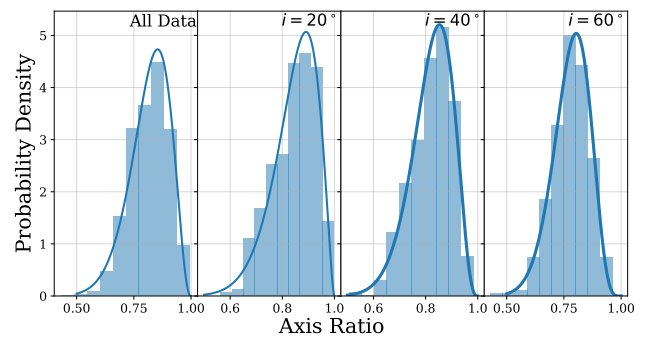


Figure 5. Axis ratios calculated from Illustris. An overall uncertainty of 0.087 was found, with similar values across inclinations of 20° , 40° , and 60° .

ate a distribution of the difference between the actual and fitted values of the position angle and thus infer an uncertainty.

We fit the resulting distributions, shown in Figure 4, with a Gaussian. Across the entire Illustris dataset, the best-fit Gaussian gives an error of 7.7° . The distribution suggests this is a conservative estimate of error, with a sharper peak in the histogram than the Gaussian fit. The approach by DiG21 assumes an error of 6° and we find that to be in line with our results.

We also analyzed our idealized mock data set, finding an error of 2.3° , in line with the findings of Häussler et al. (2007) for idealized galaxies. Given the idealized nature of this data, we would expect that features like bars, warps, and spirals would produce a larger uncertainty in a real observation. However, a good fit to the ideal data provides validation of the methods used for finding the position angle. The difference between the results from Illustris and idealized data gives an indication of the impact of non-ideal features, such as bars or warps, on the observed position angle.

Turning our attention to the errors in the axis ratio, shown in Figure 5, we find the Illustris sample is well-fit with a beta distribution across all inclination angles. The beta distribution is given by

$$f(q; \alpha, \beta) = \frac{1}{B(\alpha, \beta)} q^{\alpha-1} (1-q)^{\beta-1}, \quad (56)$$

where α and β are fitting parameters and $B(\alpha, \beta)$ is the beta function which is itself defined in terms of the gamma function,

$$B(\alpha, \beta) = \frac{\Gamma(\alpha)\Gamma(\beta)}{\Gamma(\alpha + \beta)}. \quad (57)$$

Furthermore, the variance can be computed from α and β directly

$$\sigma_q^2 = \frac{\alpha\beta}{(\alpha + \beta)^2(\alpha + \beta + 1)}. \quad (58)$$

An overall uncertainty of 0.087 was found over the entirety of the dataset. That value is improved to between $\sigma_q = 0.078$ and $\sigma_q = 0.085$ if we consider each inclination individually. However, that information would not be available in a real observation, so we opt to use the larger value in our calculations. Note, the axis ratio does not match what we would expect considering an inclined thin disk. Instead, all axis ratios tend greater than a theoretical value, with discrepancy increasing with inclination. We believe this to be an effect due to limitations in the ideal thin disk calculation, rather than an error in the fitting. The axis ratio in the calculation of Equation 51 depends on the true observed ratio, not on a thin-disk approximation.

Ultimately, we use an uncertainty of 6° in the photometric position angle and 0.087 on the axis ratio.

4.2. Idealized Mock Data

With the uncertainty in the photometric axes established, the model is then characterized on an idealized mock data set, described in Section 3.6.1. A set of fiducial values of $\gamma_\times = 0$, $\phi = 0^\circ$, $i = 40^\circ$, and $\delta_V = 10 \text{ km s}^{-1}$ were held constant across all runs, with the exception of the parameter being studied. A total of 50 realizations of the data are used for each parameter configuration.

We compared three approaches to fitting the data: (1) a nonparametric model using only kinematic data, (2) a nonparametric model using both kinematic and photometric data, and (3) a simple parametric model using only kinematic data based on Equation 53, henceforth referred to as kinematic, combined, and parametric respectively. The results are shown in Figure 6.

While varying the value of γ_\times from -0.2 to 0.2 , we find the kinematic approach generally outperforms the parametric model, with the addition of photometric data model improving over the kinematic only. The combined approach performs noticeably better at lower input shear. This is a possible indication on the limits of the approximations used in deriving the theoretical difference between the kinematic and photometric position angles, particularly in the small angle approximation used in Equation 13.

The effects of inclination are most dramatic for the parametric model, with no ability to fit at the lowest inclination angle. The kinematic model performs better than the parametric at low inclination and improves with inclination up to 60° . The combined model performs well over a wide range of inclinations, with the smallest error at mid-inclinations from 40° to 60° . Increasing to the highest inclination tested, 80° , all models have greater uncertainty than at mid-inclinations. Both nonparametric approaches give similar results at higher inclination.

Table 2. Mock Data Parameters

Parameter	Units	Range	Fiducial Value
γ_\times	-	[-0.2, 0.2]	0
ϕ	deg	[0, 75]	0
i	deg	[10, 80]	40
δ_V	km s ⁻¹	[1, 40]	10

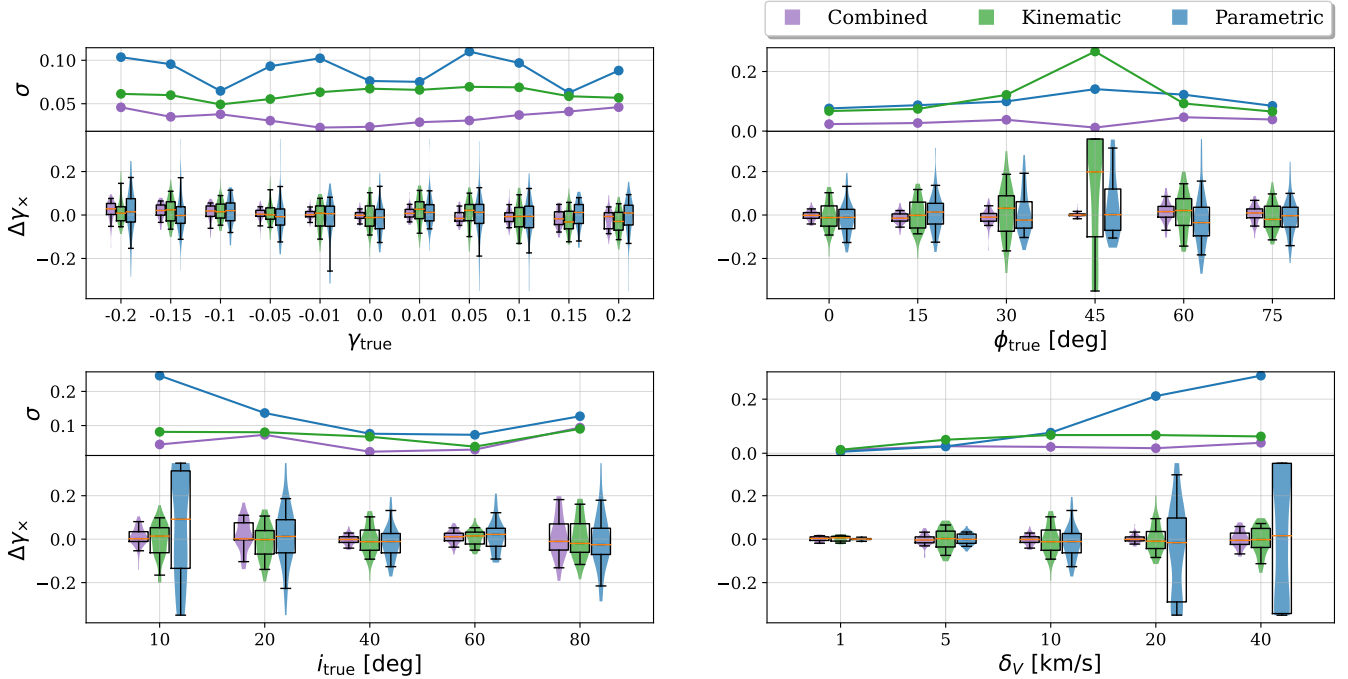


Figure 6. Characterization of the algorithm across the mock data set. A fiducial set of parameters: $\gamma_{\times} = 0$, $\phi = 0^{\circ}$, $i = 40^{\circ}$, and $\delta_V = 10 \text{ km s}^{-1}$, was used while the individual parameters were varied. Across each trial is 50 realizations of the same configuration. In the violin plots, orange lines mark the median of the data while the boxes give the interquartile range and whiskers extend to 5th and 95th percentiles. The combined model is given in purple, kinematic only in green, and a parametric kinematic model in blue.

The information available from the kinematic and photometric data varies with inclination. The information available in the photometric data is greatest at low inclinations. The apparent axis ratio increases with decreasing inclination, causing Equation 20 to diverge as q approaches unity and trend to zero as the galaxy approaches edge-on. The velocity field, however, is featureless at low inclinations. The line of sight velocity is a function of $\sin i$, with the differential velocity increasing with inclination. As the galaxy approaches edge-on, the minor axis vanishes in an infinitely thin disk model, causing the increase in uncertainty we see at $i = 80^{\circ}$.

The position angle shows dramatic effects as the angle approaches 45° . The kinematic only model is unable to fit for γ_{\times} at $\phi = 45^{\circ}$. After the algorithm fits for the position angle, application of γ_{\times} shear does not have any effect on the symmetry. With the galaxy at 45° , γ_{\times} (applied with reference to the coordinate axes) will behave as γ_{+} and only produce stretching and compressing along the galaxy axes and have no effect on galaxy symmetry. The combined model, on the other hand, seems to strongly outperform all other models at that position angle. This is *not* the result of a good fit, but rather is due to the fitting process giving $\gamma_{\times} = 0$ for any value of true shear. If we revisit Equation 25, we can see that at $\phi = 45^{\circ}$, the detector frame kinematic

position angle will also be 45° . This will push γ_{\times} to zero in Equation 18, regardless of true shear. This is the greatest difference in the two different nonparametric approaches, with both approaches failing for different reasons. However, it could be possible to construct the methods in such a way that they are sensitive to the cross component of shear in reference to the galactic axes, rather than the prescribed coordinate system. This is left for future work.

Finally, we look at the effect of noise added to the kinematic data. Gaussian noise is added at 1, 5, 10, and 20 km s^{-1} on the central pixel and scales with the inverse of the square root of the local intensity, given by Equation 54. All models show trends of a better fit at low noise and poor fit at high noise. The combined approach increasingly outperforms the other methods as noise increases. The quality of the parametric fit at extremely low-noise is probably an artifact of the mock data and parametric model using the same functional form and would not translate into performance in a real observation.

4.2.1. Effect of γ_{+}

While our technique focuses primarily on solving for γ_{\times} , real observations will contain both components of shear. We explore the impact of γ_{+} on our fit for γ_{\times} ,

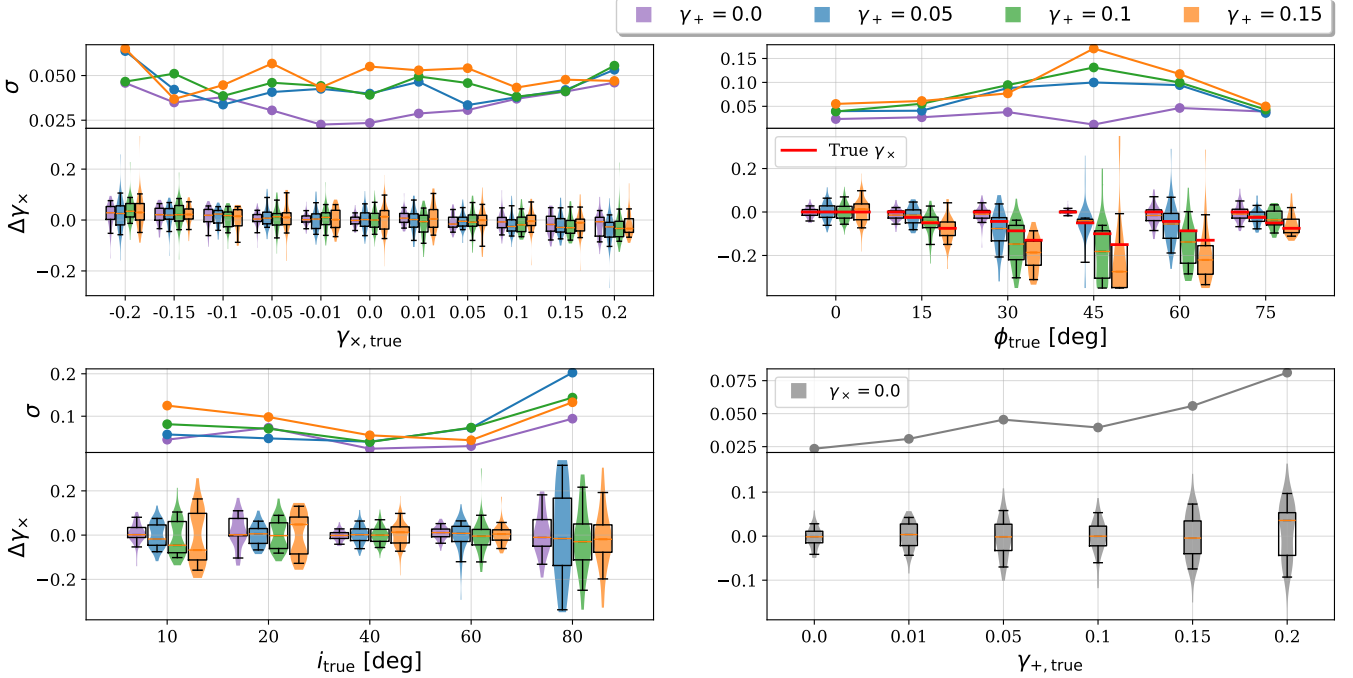


Figure 7. Impact of γ_+ on the fit for γ_x using the combined model on idealized mock data. The same fiducial set of parameters: $\gamma_x = 0$, $\phi = 0^\circ$, $i = 40^\circ$, and $\delta_V = 10 \text{ km s}^{-1}$, was used as in Figure 6. The upper-right panel shows the error in fitting γ_x with reference to a fixed detector coordinate system while the red lines indicate the true value of γ_x in a coordinate system aligned with the galaxy axes. The lower-right panel shows the effect of γ_+ on the fiducial set-up.

again using idealized mock data as in the previous section. We do not attempt to fit for γ_+ , but believe our methods could be improved by considering the parameter, which we leave for future work.

As seen in Figure 7, particularly the lower-right panel, γ_+ adversely affects the uncertainty in γ_x while having minimal impact on the median. The effects are more pronounced at both high values of γ_+ (lower-right panel) as well as γ_x (upper-left). Some slight bimodality at low inclinations could imply a systematic effect that vanishes when considering an average.

The upper-right panel of Figure 7 shows how position angle affects the fit for γ_x in the fixed detector coordinates. In these coordinates, a fiducial value of $\gamma_x = 0$ is applied with varied values for γ_+ . As the position angle approaches 45° , γ_+ applied in the fixed coordinates act as γ_x in a coordinate system aligned with the galaxy axes. This value of γ_x in the galaxy coordinates is shown with a red line at each configuration.

While γ_+ does not change the symmetry of a galaxy, it does affect our ability to treat the transformation of the photometric axes as a simple rotation, thus the derivation done in §2.1 no longer captures the full picture. Furthermore, this indicates the problem cannot be resolved by the simple inclusion of γ_+ in our transformation matrix \mathcal{A} , which is only used for symmetry transformations of the velocity field.

Overall, when fit with the combined model, the uncertainty in γ_x with $\gamma_+ < 0.2$ applied remains an improvement over both the parametric and kinematic models with no γ_+ applied. In a real observation, the shear from γ_+ is expected to be small, but efforts to include the parameter would be warranted for a complete treatment.

4.3. Illustris Data

Extending our analysis to the Illustris data, we fit the 358 halos at three inclinations each (20° , 40° , and 60°) with both the kinematic and combined models. These halos are from a $z=0$ snapshot and all expected to have $\gamma_x = 0$. Results are shown in Table 3, along with a comparison to analysis of the same data using a parametric model by DW23. Comparing the two nonparametric models, shown in Figure 8, we see the combined model shows a distinct improvement over the kinematic model. Uncertainty in the kinematic model is 0.05 considering all inclination angles and improves to 0.039 at an inclination of 60° . The combined model has an uncertainty of 0.039, improving to 0.027 at $i = 60^\circ$.

This improvement is not as dramatic as the factor of 2–6 claimed in DiG21. In that study, a parametric model of the velocity field was used similar to our mock field. However, they did not create a mock photometric

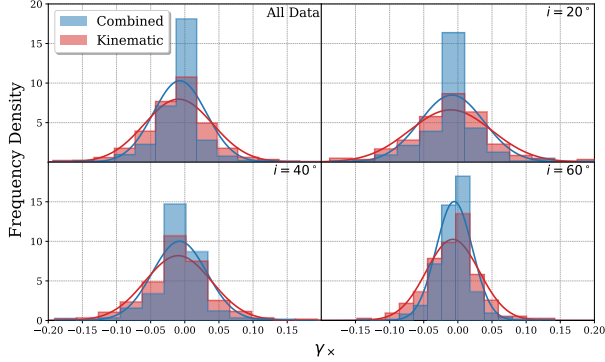


Figure 8. Comparison of the nonparametric kinematic and combined models. Adding photometric data provides a clear improvement on the fit, across all inclination angles.

observation and instead fed their model the true position angle perturbed with a 6° uncertainty. While some of the results from our fitting of the mock data are within the range of a factor of 2–6 improvement, we do not find that to be the case generally, especially not with a more realistic observation.

We analyze this Illustris data set and compare with the results from DW23 on the same data, shown in Figure 9. In that paper, they fit their distribution with a double Gaussian profile with a narrow “core”. Our method largely eliminates the broad wings seen in their distribution, such that our overall scatter is comparable to the scatter in the core of their distribution. While DW23 cites this low core uncertainty at 0.025 to 0.036, their total uncertainty is between 0.089 and 0.062, depending on inclination. Across the same inclinations,

Table 3. Comparison of Models

Model	Inclination ($^\circ$)	Mean	Median	σ
Combined	All	-0.007	-0.003	0.039
	20	-0.009	-0.003	0.047
	40	-0.008	-0.003	0.040
	60	-0.005	-0.003	0.027
Kinematic	All	-0.009	-0.006	0.050
	20	-0.011	-0.008	0.060
	40	-0.010	-0.005	0.049
	60	-0.007	-0.005	0.039
Donet (2023)	All	-0.017	-0.010	0.078
	20	-0.020	-0.012	0.088
	40	-0.018	-0.010	0.080
	60	-0.015	-0.009	0.063

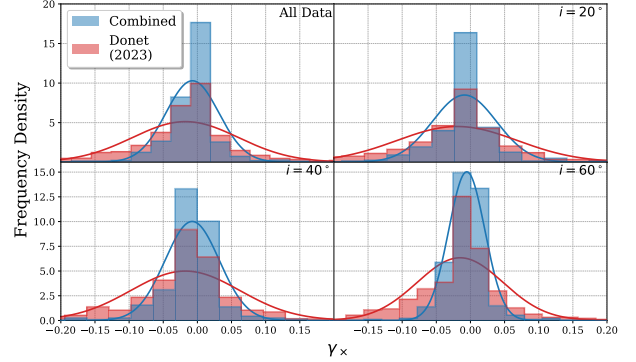


Figure 9. Comparison between the combined model and the results from DW23. The nonparametric uncertainty of 0.039 is a factor of two improvement over their parametric model.

we report a total uncertainty of 0.027 to 0.047 with an overall uncertainty of $\sigma = 0.039$ across the entire sample.

We can also see a slight bias towards negative shear, with all mean and median values being negative. The standard error in the mean of 0.001 when including all inclinations. With mean and median values of -0.003 and -0.007 , this result is significant at 3–7 sigma and matches the findings of DW23. As in that paper, we oriented all galaxies with a clockwise rotation (Z-wise orientation of spiral arms). This could produce the observed systematic bias. In a real observation averaged over an ensemble of galaxies of arbitrary orientation, we expect the bias to vanish. However, the bias could be considered in individual observations.

4.4. Moran’s I-test

Finally, we use Moran’s I-test to filter the results based on coherent patterns in the residuals. The `PySAL.esda` package returns both an I-value and a p-value for the null hypothesis of complete spatial randomness. In Figure 10, we see a definite trend in the relationship between the p and I-values, with higher I-values corresponding to lower p-values.

A good fit is one that exhibits spatial randomness, corresponding to an I-value near zero. Given the strong relationship between the p and I-values, we choose to filter the results based on p-value alone, rejecting results with $p \leq 0.001$. We can validate this choice by examining how the I and p-values relate to our fit for γ_x , Figure 11. There is a definitive trend for large value p-values and small I-values when γ_x is near its true value of 0.

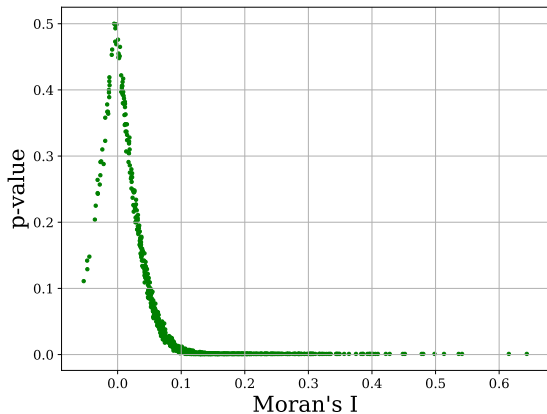


Figure 10. Relationship between Moran’s I and p-value. All statistically significant p-values, $p \leq 0.001$, correspond to relatively large I-values.

Comparing the results of the Illustris data fit with the combined model and the same results filtered with the Moran’s I-test is given in Figure 12. The 358 halos at 3 inclinations each produce a total 1074 mock observations. Of these, 472 were filtered out, leaving 602 with no consideration for inclination angle. The uncertainty in the sample was reduced from 0.039 to 0.028 with improvements at all inclination levels, shown in Table 4.

In a real observation, the most likely cause of coherent patterns in the residual will be unmodeled physical effects. Features such as warps or bars will not display the same symmetries as an ideal disk. Filtering with Moran’s I-test can help to identify targets that are poorly fit due to these features. We choose to simply eliminate these candidates from our analysis, but it is conceivably possible to eliminate the problematic features through creative masking to select the most symmetric regions of the galaxy.

We examine the halo from our sample with the largest Moran I-value. Halo 491282 was fit with a shear parameter of $\gamma_{\times} = -0.0396$ and a Moran I-value of 0.6435 and p-value of 0.001 at an inclination of 20° . As can be seen in Figure 13, there are noticeable unmodeled features

Table 4. Moran’s I filtered results.

Inclination ($^{\circ}$)	Mean	Median	σ
All	-0.007	-0.002	0.028
20	-0.009	-0.002	0.033
40	-0.007	-0.003	0.020
60	-0.003	-0.002	0.019

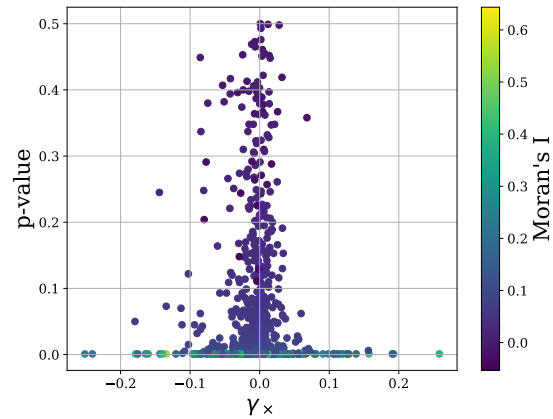


Figure 11. Results from Moran’s I-test with fitted values for γ_{\times} . Correlation between high values of Moran’s-I (low p-values) with large γ_{\times} show spatial correlation within the residuals can indicate a poor fit.

visible in the residual. While the kinematic and photometric data both look fairly innocuous, upon closer inspection of the stellar and gas column densities available from Illustris, there is distinct substructure present. These features are not symmetric and, thus, we are unable to precisely fit them with our methods.

5. SUMMARY AND CONCLUSION

In this paper, we have developed a model-independent technique for fitting the cross-component of shear, γ_{\times} , by integrating kinematic and photometric measurements. Building on the work of dBD15 and DiG21, we employed symmetry properties of a galaxy’s velocity field and photometric axes to refine the shear parameter estimation.

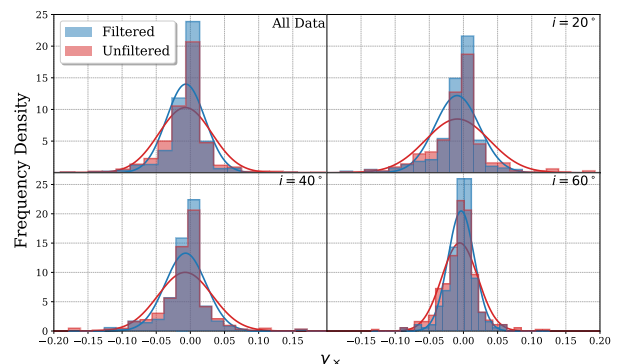


Figure 12. Histogram of results after filtering to remove sources with a p-value in Moran’s I of $p \leq 0.001$. This filtering reduced the sample size from the original 1074 (358 halos at three inclinations each) to 602 and produced and improvement on the uncertainty to $\sigma = 0.028$.

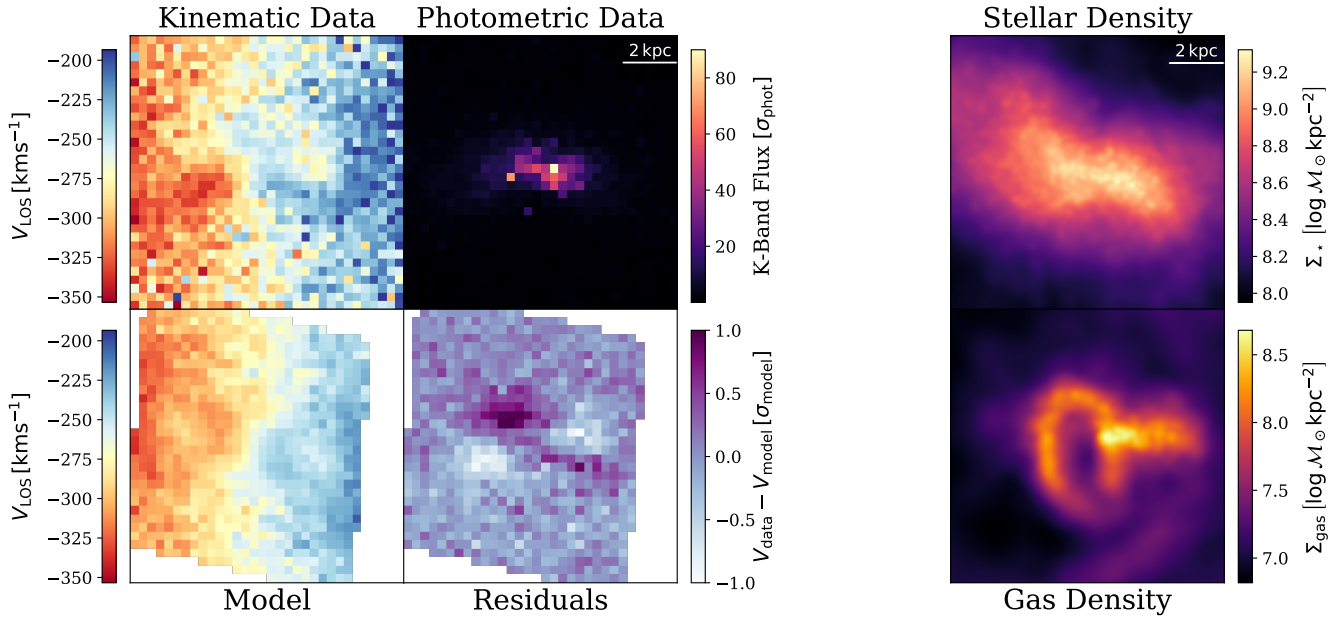


Figure 13. Visualization of Halo 491282. The data and model (left four panels) are observed at an inclination of 20° . The set of two panels on the right show the stellar and gas column densities of the galaxy observed face-on. The prominent substructure is unable to be modeled using symmetry operations and show as a pattern in the resulting residual after fitting with a shear parameter of $\gamma_x = -0.0396$. This halo was filtered out with an I-value of 0.6435. All images are 8 kpc across.

We first characterized our approach using idealized mock data, varying parameters for shear, position angle, inclination, and noise to explore the robustness and limitations of our method. Our nonparametric kinematic model showed improved precision over traditional parametric models, particularly when combined with photometric data. The addition of applied γ_+ increases scatter in the fit for γ_x with the combined model. However, for values of γ_+ up to 0.2, the uncertainty remains an improvement on both kinematic and nonparametric approaches tested without γ_+ applied.

Applying our model to a realistic dataset of 358 halos from the Illustris TNG simulations, we achieved a significant reduction in the uncertainty of γ_x , demonstrating an overall uncertainty of 0.039. These results represent a

substantial improvement over a previous parametric approach by DW23, which reported uncertainties around 0.078 on the same dataset.

Additionally, we introduced a method for identifying and discarding outliers using Moran’s I-test for spatial autocorrelation. This technique effectively filtered out halos with coherent patterns in their residuals, reducing the overall uncertainty to 0.028.

Our findings highlight the potential of integrating kinematic and photometric data in weak-lensing studies, offering a more precise measurement of weak-lensing shear.

6. ACKNOWLEDGEMENTS

We thank Jean Donet for his advice and assistance on the project, as well as his work in supplying all of the processed Illustris data files.

REFERENCES

- Bartelmann, M., & Maturi, M. 2017, *Scholarpedia*, 12, 32440, doi: [10.4249/scholarpedia.32440](https://doi.org/10.4249/scholarpedia.32440)
- Bartelmann, M., & Schneider, P. 2001, *Physics Reports*, 340, 291, doi: [https://doi.org/10.1016/S0370-1573\(00\)00082-X](https://doi.org/10.1016/S0370-1573(00)00082-X)
- Blain, A. W. 2002, *The Astrophysical Journal*, 570, L51, doi: [10.1086/341103](https://doi.org/10.1086/341103)
- de Burgh-Day, C. O., Taylor, E. N., Webster, R. L., & Hopkins, A. M. 2015, *Monthly Notices of the Royal Astronomical Society*, 451, 2161, doi: [10.1093/mnras/stv1083](https://doi.org/10.1093/mnras/stv1083)
- DiGiorgio, B., Bundy, K., Westfall, K. B., Leauthaud, A., & Stark, D. 2021, *The Astrophysical Journal*, 922, 116, doi: [10.3847/1538-4357/ac2572](https://doi.org/10.3847/1538-4357/ac2572)

- Donet, J., & Wittman, D. 2023, *The Astrophysical Journal*, 945, 88, doi: [10.3847/1538-4357/acbb70](https://doi.org/10.3847/1538-4357/acbb70)
- Foreman-Mackey, D., Hogg, D. W., Lang, D., & Goodman, J. 2013, *Publications of the Astronomical Society of the Pacific*, 125, 306
- Goodchild, M. F. 1986, *Spatial Autocorrelation*, CATMOG 47 (Norwich: Geo Books)
- Gurri, P., Taylor, E. N., & Fluke, C. J. 2020, *Monthly Notices of the Royal Astronomical Society*, 499, 4591, doi: [10.1093/mnras/staa2893](https://doi.org/10.1093/mnras/staa2893)
- Häussler, B., McIntosh, D. H., Barden, M., et al. 2007, *The Astrophysical Journal Supplement Series*, 172, 615
- Krajnović, D., Cappellari, M., De Zeeuw, P. T., & Copin, Y. 2006, *Monthly Notices of the Royal Astronomical Society*, 366, 787
- Krajnović, D., Emsellem, E., Cappellari, M., et al. 2011, *Monthly Notices of the Royal Astronomical Society*, 414, 2923
- McKay, T. A., Sheldon, E. S., Racusin, J., et al. 2001, Arxiv preprint astro-ph/0108013
- Morales, M. F. 2006, *The Astrophysical Journal*, 650, L21, doi: [10.1086/508614](https://doi.org/10.1086/508614)
- Moran, P. A. 1948, *Journal of the Royal Statistical Society. Series B (Methodological)*, 10, 243
- Nelson, D., Springel, V., Pillepich, A., et al. 2019, *Computational Astrophysics and Cosmology*, 6, 1
- Rey, S. J., & Anselin, L. 2007, *The Review of Regional Studies*, 37, 5
- Troxel, M. A., MacCrann, N., Zuntz, J., et al. 2018, *Physical Review D*, 98, 043528
- Umetsu, K. 2020, *The Astronomy and Astrophysics Review*, 28, 7
- Umetsu, K., Medezinski, E., Nonino, M., et al. 2014, *The Astrophysical Journal*, 795, 163